nature materials

Article

https://doi.org/10.1038/s41563-024-02035-3

Antagonistic-contracting high-power photo-oscillators for multifunctional actuations

Received: 8 January 2024

Accepted: 25 September 2024

Published online: 24 October 2024

Check for updates

Yusen Zhao[1], Zixiao Liu[1], Pengju Shi[1], Chi Chen[1], Yousif Alsaid[1], Yichen Yan[1] & Ximin He[1,2]

High-power autonomous soft actuators are in high demand yet face challenges related to tethered power and dedicated control. Light-driven oscillation by stimuli-responsive polymers allows for remote energy input and control autonomy, but generating high output power density is a daunting challenge requiring an advanced material design principle. Here, inspired by the flight muscle structure of insects, we develop a self-oscillator based on two antagonistically contracting photo-active layers sandwiching an inactive layer. The actuator produces an output power density of 33 W kg^{-1}, 275-fold higher than other configurations and comparable to that of insects. Such oscillators allow for broad-wavelength operation and multifunction integration, including proprioceptive actuation and energy harvesting. We demonstrate high-performance flapping motion enabling various locomotion modes, including a wing with a thrust-to-weight ratio of 0.32. This work advances autonomous, sustained and untethered actuators for powerful robotics.

There is a growing demand for high-power-output soft actuators in robotics, aimed at facilitating rapid motion across terrestrial, marine and aerial domains[1]. In some particular scenarios such as microscale aerial vehicles, this need becomes even stringent and urgent, because the power density needs to surpass a specific threshold (>29 W kg^{-1}) to overcome its own weight and initiate lift-off[2,3]. Typical robots rely on either tethered or onboard power supplies as the energy source, complemented by sophisticated computer-programmed control systems to perform basic tasks. Alternatively, stimuli-responsive polymers that can interact with and self-adapt to their environment offer promising material opportunities. These polymers can be fuelled and deformed by remote energy inputs[4,5]. However, to generate repetitive back-and-forth motion, this typically necessitates manual intermittent stimuli, and the motions are slow (>1 s)[6,7]. These characteristics pose a challenge to the realization of autonomous and high-power robotic motion.

Emulating the inherent sensing–diagnosis–actuation feedback found in biological systems[8,9], light-driven self-excited oscillation has emerged as a promising approach for untethered autonomous actuators[10–12]. With this strategy, remote and constant photo-energy can generate reciprocal actuation and regulate directional locomotion, inherently operating without the need for manual intervention[12–15]. The photo-actuation involves complicated time-varying multiphysics, by either photo-thermal-mechanical[15] or photo-chemical-mechanical[16] mechanisms. During the dynamic oscillation, the photo-active film contracts upon illumination, causing rapid bending. When overbent, the tip self-blocks light, leading to relaxation and unbending for the next oscillation cycle. Thus, a built-in negative feedback loop is formed through the dynamic competition of photo-induced bending and self-shadowing-induced unbending[11,12]. To initiate the self-excited oscillatory motion, this feedback has to be amplified above a specific photo-energy input threshold, during which the photo-thermal heating or photo-chemical effect fuels the bending of active materials and sufficiently compensates the energy dissipation arising from viscoelastic damping and air resistance. Over the decades, this intricate

[1]Department of Materials Science and Engineering, University of California, Los Angeles, Los Angeles, CA, USA. [2]California Nanosystems Institute, Los Angeles, CA, USA. e-mail: ximinhe@ucla.edu

https://doi.org/10.1038/s41563-024-02035-3

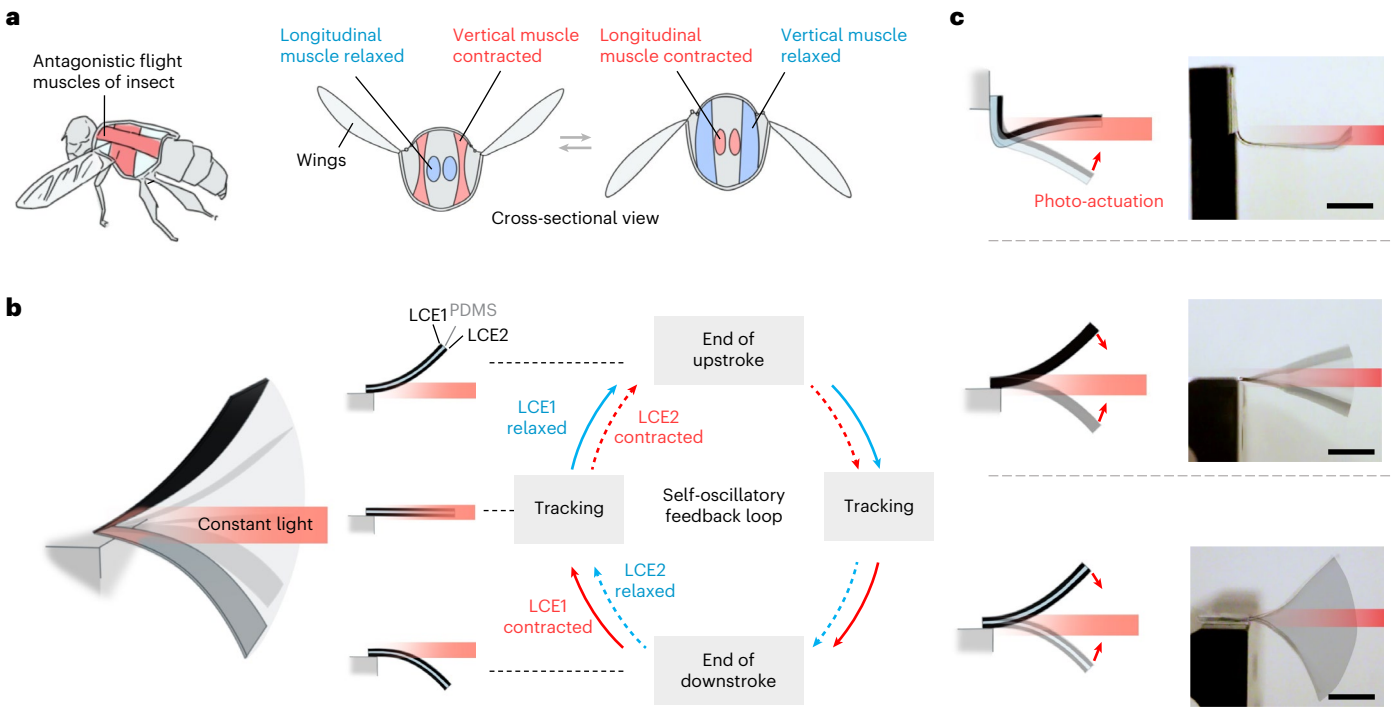

Fig. 1 | FLaPTOR design schematics. a, An illustration of an insect's wing stroke, showing antagonistic muscles in the process of contraction (red) and relaxation (blue). **b**, An illustration of the operation mechanism of the FLaPTOR. Two photo-responsive LCE films laminated on both sides (LCE1, LCE2) are used to perform antagonistic actuation during self-excited oscillation under constant light input. **c**, Structural configuration comparisons of LPBO (top), an LMO (middle) and the LCE/PDMS/LCE trilayer FLaPTOR (bottom). Red arrows indicate the direction of photo-actuation during the upstroke and downstroke. Scale bars, 1 cm.

process has been extensively studied and comprehended through a combination of experiment and simulation[17–19]. Our previous works have contributed to unveiling the coupling and initiation process of such photo-thermal-mechanical oscillation by the design of highly photo-thermally efficient and highly active materials for sustainable energy input applications[11,12,20,21].

In terms of mechanical output performance, light-driven oscillators on the insect scale (10–100 mm) can generate power densities typically below 0.5 W kg^{-1}, falling short of the remarkable performance of the flight muscles of insects (>29 W kg^{-1})[22], piezoelectric actuators (>150 W kg^{-1})[2] and dielectric elastomer actuators (2–600 W kg^{-1})[23,24]. Although researchers have developed high-frequency oscillators, the sub-millimetre sizes are too small for further integration and the design of a comprehensive robot system[25,26]. Fundamentally, there remains a notable lack of understanding regarding the material–property relationships and design principles crucial for high-power-output oscillations, such as the modulus–power relationship, viscoelasticity–damping relationship, thermal effect, feedback-loop modulation, geometry effect and so on. Addressing these design challenges would prove advantageous for the development of highly robust and powerful robots capable of diverse tasks such as walking and swimming and potentially the achievement of flapping wings. Additionally, current state-of-the-art oscillators based on liquid crystalline networks and hydrogels require single-wavelength light operation[25], light polarization[16] and under-water conditions[12], which limit their practical operation using ambient energy such as outdoor solar light. Furthermore, most oscillators consist of a monolithic layer, making it hard to achieve system-level function integration, such as sensing, energy harvesting and robotic locomotion.

Therefore, a distinct design of oscillators is needed for the development of high output power with operation across a broad spectrum of non-polarized light while offering multifunctionality. Drawing inspiration from the structure of insect flight muscles, which feature antagonistic muscle pairs that contract and relax asynchronously, we propose that mechanical coupling across opposite muscle tissues can boost the mechanical output power (Fig. 1a)[27,28]. In addition, regarding the system functional design, the common robotic design maximizes the active materials for deformation and minimizes the inactive material mass, aiming to enhance the overall output power density of the system[29,30].

In this study, we designed a light-driven oscillator that imitates the antagonistic muscle structure of insect wings. Unlike common functional design, we intentionally inserted an inactive material within the active materials to form a trilayer, active–inactive–active structure, as opposed to an entirely active, monolithic material. Counterintuitively, the trilayer with a certain portion of inactive material could produce an exceptionally high output power density of 33 W kg^{-1}, which is comparable to that of insect flight muscles, and up to 275-fold higher than that of counterparts with other configurations. Specifically, the trilayer construct was composed of two photo-responsive liquid crystalline elastomer (LCE) layers for antagonistic contraction, sandwiching an inactive elastic polydimethylsiloxane (PDMS), being termed a flapping LCE-and-PDMS trilayer oscillatory robot (FLaPTOR). The FLaPTOR exhibited broad-spectrum operation and allowed for multiple functionalities, such as proprioceptive actuation and energy harvesting. The flapping actuator also enabled high-performance robotic motions, including sailboats, bi-directionally moving walkers and a flapping wing with an average lift force of 147 μN and a thrust-to-weight ratio of 0.32, marking a major milestone in the advancement of autonomous, self-sustained and untethered flapping actuators at the insect scale.

Results

Design rationale

The primary intent of this work is to establish a design principle for self-shadowing-based light-driven self-oscillation to achieve high

https://doi.org/10.1038/s41563-024-02035-3

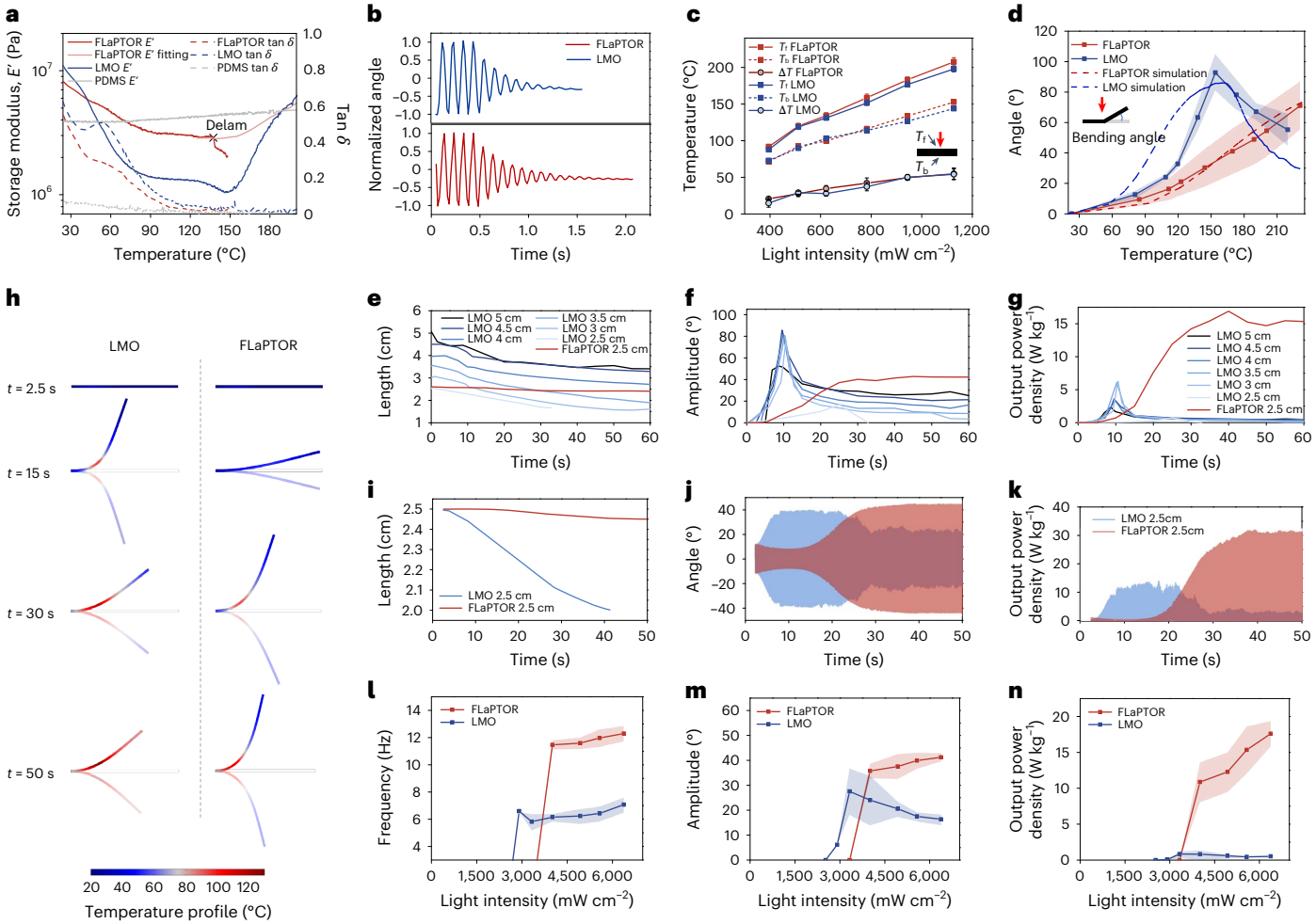

Fig. 2 | Fundamental studies of the performance improvement of FLaPTOR compared with LMO. a, The storage modulus and tan δ of two configurations during a temperature ramp. The modulus above 140 °C was fitted using the LCE and PDMS data because the LCE was delaminated (Delam) from PDMS after 140 °C owing to an overly high thermally induced stress mismatch between the LCE and PDMS. **b**, The normalized angle changes of FLaPTOR and LMO after turning off the light. **c**, The thermal profile of two configurations under different input light intensities ($N = 3$). T_f and T_b are the temperature on the front and back side of the sample, respectively. **d**, The thermomechanical bending at different surface temperatures on the illuminated side of LCE by experiment (solid curves with symbols, and shaded areas representing the s.d. of the measured values with $N = 3$) and simulation (dashed curves). Inset in **c**,**d** shows the measurement method and red arrows indicate the light direction. **e**–**k**, The length (**e** and **i**), amplitude (**f** and **j**) and output power density (**g** and **k**) obtained by time-dependent oscillation tests (**e**–**g**) and simulations (**i**–**k**) conducted on the LMO and the FLaPTOR. The light intensity was 5,580 mW cm^{-2}. The original length of the LMO was changed from 5 cm to 2.5 cm. **h**, The beam displacement and thermal profile over time (t) generated by simulation. To decouple the length shortening effect, the oscillation performance was evaluated by using a longer length and ensuring the length during oscillation was consistently 2.5 cm. **l**–**n**, The measured frequency (**l**), amplitude (**m**) and output power density (**n**) with shaded areas representing the s.d. of the measured values with $N = 5$.

mechanical output, which is desired for robotics (Fig. 1b). One challenge is that employing self-oscillation necessitates lower-stiffness materials to facilitate easier overbending and create out-of-equilibrium motion, but such softer materials lead to lower frequency and are suboptimal for generating high output power. Existing splayed[31] and bilayer[32] structures of oscillators yield inadequate power density owing to their single upstroke photo-actuation process (Fig. 1c). Instead, a bi-directional photo-actuation mode enhances the energy conversion, because photo-active materials can harvest photo-energy during both the upstroke and downstroke. Specifically, we utilized a geometrically and chemically symmetric structure[33,34] and produced thermal gradient across the thickness direction. However, symmetric photo-thermal liquid crystalline network films were unable to bend, potentially owing to their low thickness, low actuation strain and fast heat transfer[14,31,32,35,36]. To generate a large thermal gradient, we increased the thickness and thus the thermal diffusion time scale ($\tau \propto t^2/D$, where t is the thickness and D is the thermal diffusivity). To achieve deformation with a larger thickness, we developed a LCE with high photo-thermo-mechanical energy transduction[11,13]. To create an enhanced strain mismatch across the thickness for better bending, we inserted a passive PDMS layer in the middle (Fig. 1b,c). We systematically investigated the impact of the inclusion of inactive components on such a highly complex out-of-equilibrium system, considering that the overall performance is also governed by the resonant frequency, the system damping, the structural stability and the amplification of the closed-loop feedback.

The FLaPTOR was carefully fabricated by first synthesizing the LCE and PDMS independently, then sandwiching them together using silicone glue. A silica coating was vapour-phase deposited onto each surface to enhance adhesion (Supplementary Figs. 5 and 6).

Enhancement of the output power density

The FLaPTOR versus an LCE monolithic oscillator. Both the FLaPTOR and the LCE monolithic oscillator (LMO)[16,25] enable bi-directional photo-actuation, while the FLaPTOR has PDMS as a middle layer (Supplementary Fig. 7 and Supplementary Table 2). Surprisingly, the FLaPTOR demonstrated a maximum output power density of 23 W kg^{-1},

which was 14-fold higher than that of the LMO (1.6 W kg^{-1}) (Fig. 2n and Supplementary Video 1). To investigate this unusual improvement, we first conducted fundamental material characterizations in the static state. Mechanically, the FLaPTOR showed a higher storage modulus and lower viscoelasticity (lower tan δ, known as the damping factor), which were attributed to the stiff and elastic PDMS layer (Fig. 2a). According to oscillation theory[31], a higher modulus leads to a higher resonant frequency (which scales with $E^{0.5}$) and a higher power density P_m (which scales with f^3; Supplementary Section 3), where l is the length, A is the angular amplitude, f is the frequency, a is the thickness, E is the modulus and ρ is the density.

$$P_m = \frac{\sqrt{2}}{12} l^2 A^2 (2\pi f)^3$$

$$f = \frac{1.01a}{2\pi l^2}\sqrt{\frac{E}{\rho}}.$$

A lower viscoelasticity will induce the oscillator to be underdamped and efficiently utilize the photo-energy input for mechanical output. This was verified by the quality factor (Q), where the Q factor of the FLaPTOR was 9, much larger than that of the LMO, which was 5.7 (Fig. 2b). In terms of their thermal properties, both the FLaPTOR and the LMO showed a similar temperature profile under the same light intensity, indicating similar heat transport and dissipation behaviours (Fig. 2c). This similarity is attributed to the comparable thermal conductivity of PDMS (0.15 W m^{-1} K^{-1})[37] and LCE (0.24 W m^{-1} K^{-1})[38]. Furthermore, we examined the static thermomechanical actuation using near-infra-red light from one side and conducted a simulation accordingly (Supplementary Section 4.2). LMO initially exhibited a higher bending angle, but further increasing the light intensity caused it to unbend (Fig. 2d)[39]. This reduction in bending angle was attributed to a flattened actuation strain (ε) above 150 °C and a decreasing strain gradient ($\delta\varepsilon/\delta T$) with temperature T (Supplementary Fig. 8). As a result, the temperature–angle curve exhibited a negative slope, which is detrimental to the production of amplification of oscillation (Supplementary Fig. 9). In contrast, the FLaPTOR demonstrated a more linear and higher bending angle up to 200 °C, which was also verified by simulation (Fig. 2d). We considered that PDMS functioned as a buffering material, where the negative effect of LCE at higher temperature will be diluted, including a stiffness increase and a response decrease. This linear thermomechanical curve of the FLaPTOR facilitated the oscillation amplification.

The FLaPTOR versus LCE-PDMS bilayer oscillator. We then conducted a dynamic study on the time-dependent evolution of the oscillation after light exposure (Fig. 2e–k and Supplementary Video 2) by experiment and COMSOL Multiphysics. We found that the LMO length reduced over time by more than 30% in 1 min, but the FLaPTOR length remained steady over time. This is because the heat was transferred from the surface to the middle of the actuator. Then, the LMO will shrink universally. In the FLaPTOR, however, the rigid PDMS resisted the contraction of the LCE. Such length shortening could impede the oscillatory behaviour owing to the higher bending stiffness[12]. Secondly, we observed an amplitude/power decay for the LMO from 10 s but steady amplitude/power enhancement for the FLaPTOR. The performance decay of the LMO could be attributed to the thermal transfer into the middle area with thermomechanical angle reduction. Moreover, we decoupled the length shortening effect by using a longer initial length and fixed the length during oscillation to be 2.5 cm, the same as the length of the FLaPTOR. Interestingly, the frequency, amplitude and output power density of the FLaPTOR with the same oscillating length still outperformed those of LMOs (Fig. 2l–n). To gain insight into this output power difference, we admitted that the active–inactive–active structure will sacrifice actuation performance in the static state. However, in the dynamic in-equilibrium system, multiple factors finally contribute to the net performance enhancement, as supported by finite element simulation (Supplementary Fig. 10), in particle (1) the high PDMS stiffness increased the frequency, (2) the low viscoelasticity reduced the oscillator damping, (3) the linear thermomechanical bending curve amplified the closed-loop feedback and (4) the inactive and stiff PDMS stabilized the oscillating length.

The LCE-PDMS bilayer oscillator (LPBO) exhibited single-direction photo-actuation (Supplementary Fig. 7 and Supplementary Table 2). By controlling the same actuator thickness, LPBO could only produce a maximum power density of 0.1 W kg^{-1} (Supplementary Fig. 11), which was more than two orders of magnitude lower than that of the FLaPTOR with its bi-directional photo-actuation. Fundamentally, the FLaPTOR enabled photo-thermal actuation during the whole cycle instead of during a half cycle as in the LPBO. The shortening of one LCE layer facilitated the relaxation of another LCE layer, in contrast to the reliance solely on the thermal relaxation of the upper LCE layer in the LPBO. This effect improves the flapping speed to a higher value, which is proportional to the angular frequency and angular amplitude, and helps improve the output power. Furthermore, the LPBO suffered from tip coiling at higher light intensity, indicating that the system had exceeded the upper limit of balance between the power input and the mechanical energy release[15].

LCE structure–property–performance development for the FLaPTOR

Tailoring the chemistry of the LCE and the structural design of FLaPTORs plays a crucial role in achieving high-power-density oscillation, which requires both high frequency and high amplitude. We explored three distinct predominant fabrication methodologies for LCEs and examined the resulting thermomechanical properties. Specifically, we firstly utilized thiol-acrylate Michael addition polymerization to obtain randomly oriented LC oligomers. Then, the polydomain oligomers were aligned in a single direction and the networks were permanently fixed by photo-crosslinking. The three fabrication methods we used are illustrated in Fig. 3a: (1) liquid-like oligomers extruded through direct ink writing (DIW), followed by thiol–ene photo-crosslinking chemistry (DIW-TE)[40], (2) solid oligomers being mechanically stretched (Supplementary Fig. 12) and crosslinked via thiol–ene photo-crosslinking (MeS-TE) and (3) solid oligomers being mechanically stretched with diacrylate photo-crosslinking (MeS-TA)[41]. We studied the effects of different monomers, spacers and crosslinkers for each synthesis method (Fig. 3a and Supplementary Table 3). The thermomechanical properties of the LCEs are governed by the interaction of the diverse chemical components of the segments and their packing structures, which modulate the liquid crystal phase morphology[41]. Among the fabrication methods studied, the MeS-TA approach, which employed RM257 as the mesogen and 1,6-hexanedithiol as the spacer, exhibited a storage modulus of 21.5 MPa at room temperature, an actuation strain of 64% at 200°C, an actuation stress of 1.2 MPa at 140 °C and a work capacity of 311 kJ m^{-3} under a load of 500 kPa at 200 °C, outperforming other fabrication methods, formulations and reported LCEs (Fig. 3c and Supplementary Table 4). This improved performance can be attributed to (1) the incremental mesogen orientation obtained through mechanical stretching, (2) the increased modulus achieved while maintaining the actuation strain by employing acrylate crosslinking[40] and (3) the phase segregation of rigid mesogens and spacers[41].

Then, we investigated the oscillatory performance using these LCEs and assembled them into FLaPTORs (Supplementary Video 3). The study aimed to explore the relationship between the thermomechanical properties and the oscillatory performance for different LCEs. We observed that a high modulus and high actuation strain make positive contributions to the enhancement of the output power, according to our empirical correlation analysis (Supplementary Figs. 14 and 19). Among all the LCE formulations, the MeS-TA methodology with RM257-HDT exhibited the highest output power, consistent with the LCE thermomechanical study above (Fig. 3c–g). Furthermore, the

https://doi.org/10.1038/s41563-024-02035-3

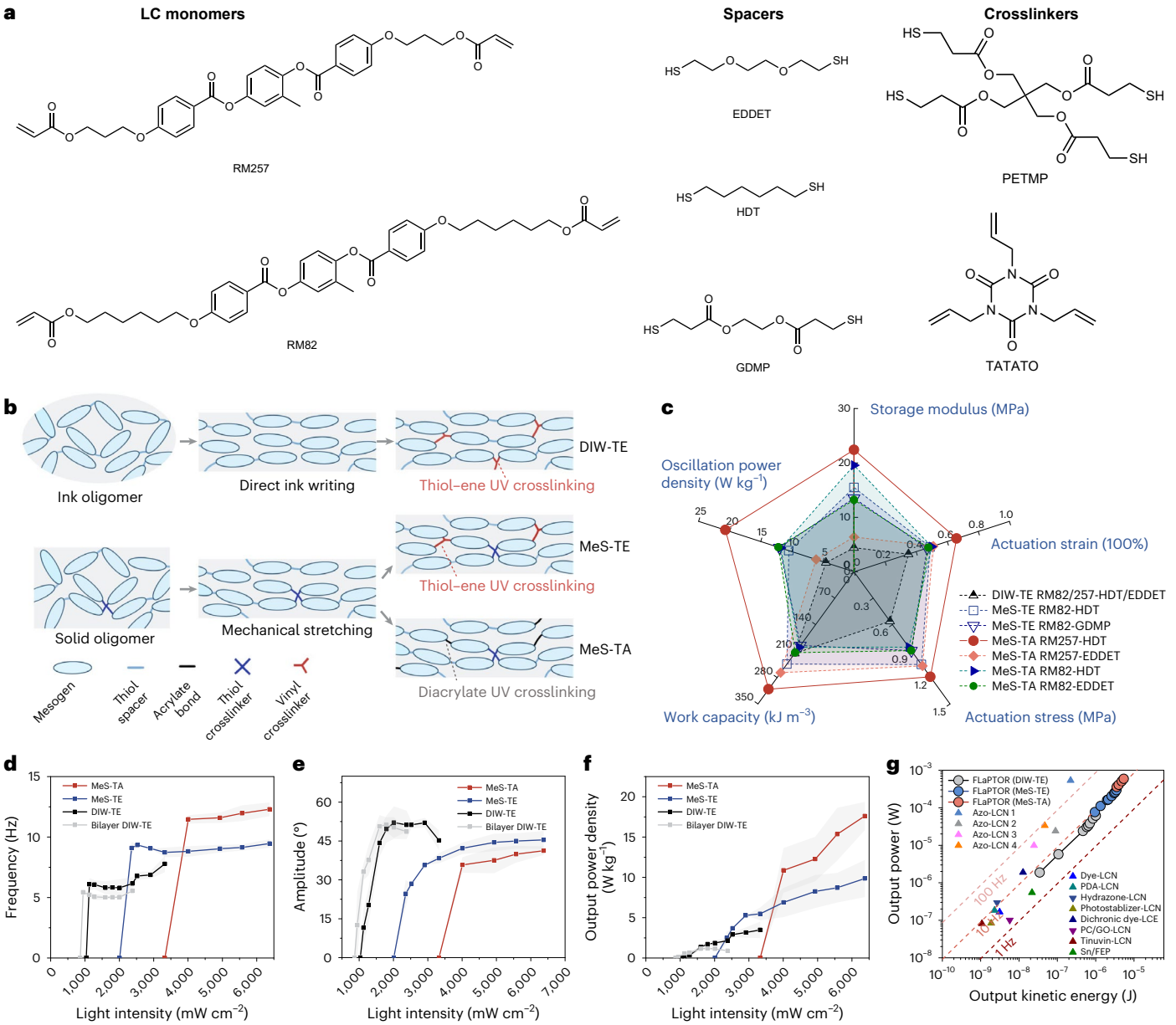

Fig. 3 | The structure–property–performance relationship of the FLaPTOR. **a**, The compositions of the LCEs. EDDET, 2,2-(ethylenedioxy)diethanethiol; GDMP, 1,4-butanediol bis(thioglycolate); HDT, 1,6-hexanedithiol; PETMP, pentaerythritol tetrakis(3-mercaptopropionate); TATATO, 1,3,5-triallyl-1,3,5-triazine-2,4,6(1*H*,3*H*,5*H*)-trione. **b**, Illustrations of the polymerization procedures for the different LCE synthesis methodologies. **c**, The thermomechanical properties of the LCEs and the oscillatory performance after their fabrication into FLaPTORs. The geometrical configurations were a 120/50 LPBO bilayer using DIW-TE (baseline), 120/134/120-2 cm FLaPTOR for DIW-TE, 115/320/115-2.5 cm for MeS-TE and 145/320/145-2.5 cm for MeS-TA. Detailed analysis is presented in Supplementary Information. **d**–**f**, The frequency (**d**), amplitude (**e**) and oscillatory power density (**f**) as functions of the light intensity. **g**, The output power versus the kinetic energy, showing that the FLaPTOR design outperformed reported oscillators. FEP, fluoroethylene propylene; LCN, liquid crystalline network; GO, graphene oxide; PC, polycarbonate; PDA, polydopamine. All shaded areas represent the s.d. of the measured values ($N = 5$).

output kinetic energy and the output power of the FLaPTORs surpassed other reported light-driven oscillators, suggesting that the chemical development and the unique structural configuration facilitate efficient energy transduction and mechanical output (Fig. 3g and Supplementary Table 5).

We also studied the effects of geometrical factors, including the LCE thickness, the PDMS thickness and the total oscillator length, on the oscillatory performance of our FLaPTORs by experiment and finite element simulations (Fig. 4 and Supplementary Figs. 15–18, respectively). Consistent with oscillation theory, a higher light intensity produced an unaltered frequency (a feature of resonant actuation), an increased amplitude and a higher output power density[31]. In addition, thicker PDMS and/or LCE layers required a higher onset light intensity for initiating oscillation, suggesting that increased energy was needed to overcome resistive forces such as damping (Fig. 4a–f). While thicker films resulted in increased oscillation frequency, they compromised the amplitude at a given light intensity owing to the increased moment of inertia. Moreover, excessively high light intensity (>6,500 mW cm^{-2}) led to LCE fracture, because PDMS imposed a geometrical constraint from LCE contraction. When the total thickness was fixed and the PDMS/(PDMS + LCE) thickness ratio was varied, increasing the PDMS thickness ratio caused a right shift of the operation window due to the reduction in LCE fraction for photo-responsive actuation, but the maximum output power density remained similar (Fig. 4g–i). Furthermore,

https://doi.org/10.1038/s41563-024-02035-3

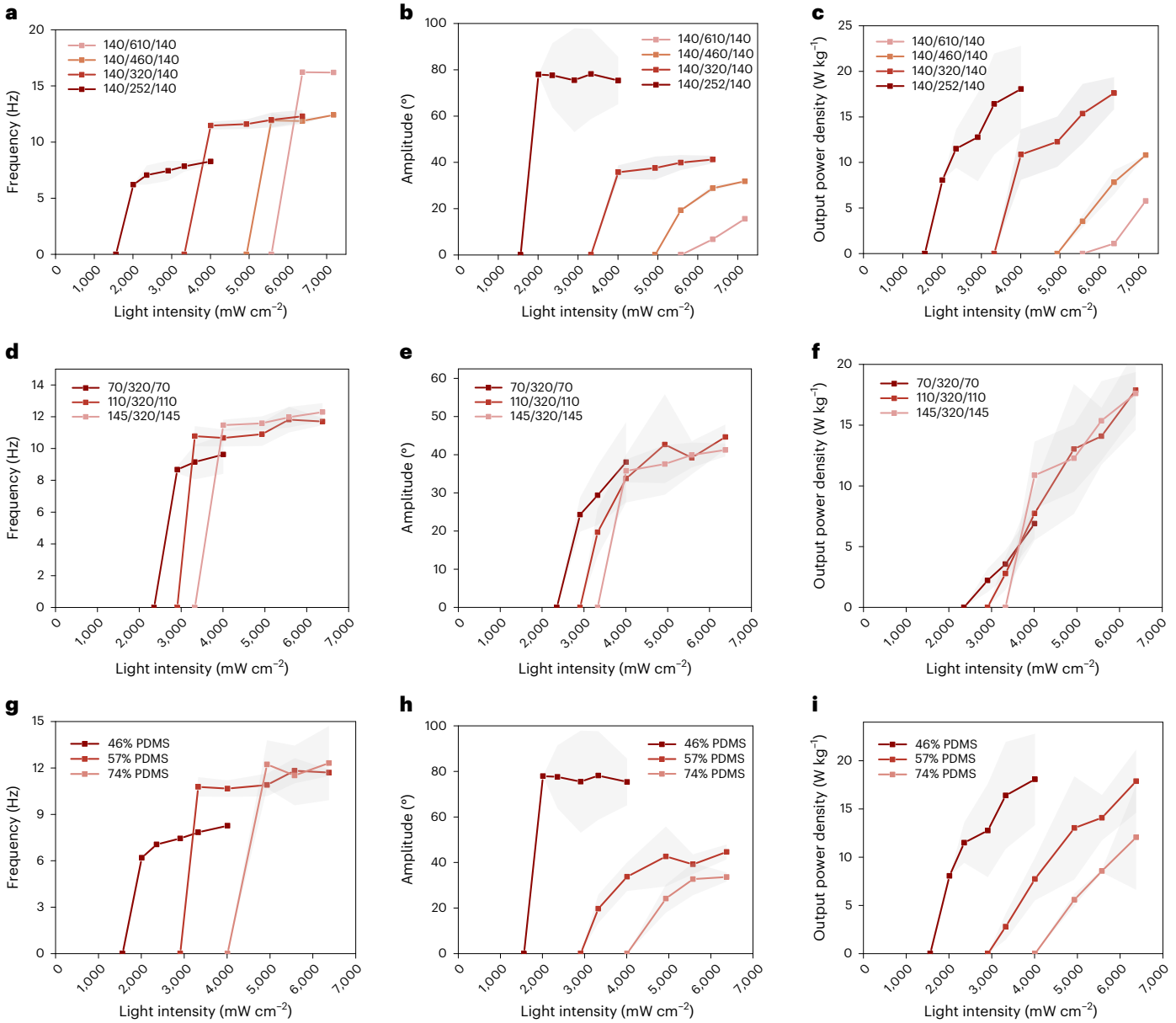

Fig. 4 | Geometrical effects on the FLaPTOR performance. The LCE layers were controlled to be 70–145 µm in thickness, and the PDMS middle layers were controlled to be 50–610 µm in thickness. **a**–**i**, The influences of the PDMS thickness (**a**–**c**), the LCE thickness (**d**–**f**) and the PDMS/(PDMS + LCE) thickness ratio (**g**–**i**) at a fixed total thickness of 600 µm on the frequency (**a**, **d** and **g**), amplitude (**b**, **e** and **h**) and output power density (**c**, **f** and **i**). Shaded areas represent the s.d. of the measured values ($N = 3$).

decreasing the oscillator length could increase the oscillation threshold and boost the overall output power density, but there is more risk of fracturing due to overly high energy input (Supplementary Fig. 18). Through systematic studies of the LCE formulation, thickness and length, we determined that the optimal geometry was 145/320/145-2.5 cm (using the nomenclature *x*/*y*/*x*-*z* for the FLaPTOR geometry, where *x* is the PDMS thickness in micrometres, *y* is the PDMS thickness in micrometres and *z* is the FLaPTOR length in centimetres) and the use of the MeS-TA methodology with RM257-HDT. This FLaPTOR yielded a frequency of 13 Hz, an amplitude of 42° and a maximum power density of 33 W kg^{-1}, comparable to the flight muscle of insects.

Multifunctionality

By embedding candle soot into the LCE layers, the FLaPTOR could undergo oscillatory motion upon a broad spectrum of light, ranging from blue to near-infra-red, and simulated solar light (Fig. 5a and Supplementary Video 4). In particular, the oscillating frequency remained consistent under different wavelengths (Fig. 5b).

Owing to the unique sandwich structure, we have the capability to functionalize the actuation for system integration. First, the FLaPTOR was incorporated with a gold electrode within the PDMS to achieve proprioception actuation, suggesting that the oscillator can monitor its own deformation in real time (Fig. 5c, Supplementary Fig. 16a and Supplementary Video 5). The gold electrode, serving as a sensing layer, is lengthened and contracted during oscillation, leading to periodic piezoresistive changes. No electrical disconnection was observed within the 2,380–2,900 mW cm^{-2} light intensity range. The resistance changes matched the angular oscillations, with consistent frequency. By increasing the light intensity, the sensor had increased resistance due to greater deformation. Furthermore, the proprioceptive performance remained stable over ~3,000 continuous cycles (Fig. 5d,e and Supplementary Fig. 20).

https://doi.org/10.1038/s41563-024-02035-3

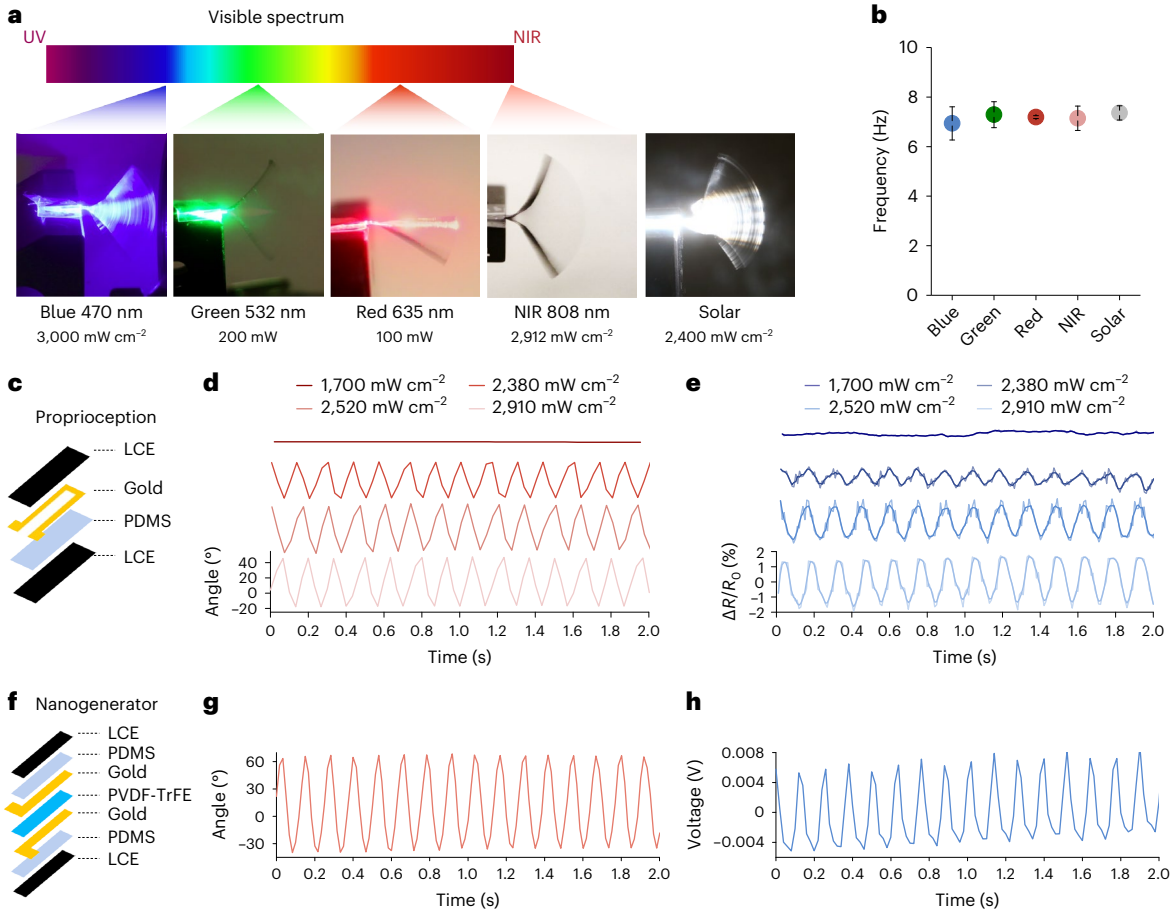

Fig. 5 | The multifunctionality of the FLaPTOR. a, Broad-spectrum operation of oscillation. NIR, near-infra-red. **b**, The frequency of oscillation under different wavelengths of light. Error bars represent the s.d. of the mean values with $N = 3$. **c**, A schematic representation of a proprioceptive oscillator. **d**,**e**, The angle changes (**d**) and normalized resistance changes (**e**) of the oscillator over time upon different light intensities. **f**, A schematic representation of a piezo/pyroelectric nanogenerator integrated into the oscillator. **g**,**h**, The angle changes (**g**) and voltage changes (**h**) of the nanogenerator over time.

Another functionalization of the FLaPTOR for system integration is electrical energy harvesting, where we embedded pyroelectric and piezoelectric layers made by poly(vinylidene fluoride-co-trifluoroethylene) (Fig. 5f and Supplementary Figs. 2 and 21). The time-dependent potential change generated by the device demonstrated frequency consistency with the angle change of the oscillation (Fig. 5g,h). Under oscillatory motion, the peak potential could reach ~10 mV, owing to the piezoelectric effect from the dynamic strain change and the pyroelectric effect from the dynamic temperature change of the actuator hinge. Our design is a fully integrated photo-electric converting device with a light-driven oscillation mechanism, marking a breakthrough in smart actuators for autonomous energy harvesting[42,43].

Soft robotics

First, we leveraged the high mechanical output of the FLaPTOR to propel a sailboat, integrating it with a passive wing. Controlled by the light intensity and the flapping amplitude, the boat's speed reached 1.6 mm s^{-1}, outperforming previous flapping-based systems by 3–5-fold[12] (Fig. 6, Supplementary Figs. 3 and 22 and Supplementary Video 6). Subsequently, we applied the FLaPTOR wing to a rail-assisted walker, enabling forwards and backwards walking motions (Fig. 6c,d and Supplementary Video 7). The directional movement is governed by friction asymmetry, exhibiting speeds of 2.5 mm s^{-1} forwards and 0.76 mm s^{-1} backwards, with faster forward movement due to flapping wing propulsion[7] (Supplementary Fig. 23).

Owing to the high output power of the FLaPTOR, we further studied the potential of the FLaPTOR wing for flapping wing microscale aerial vehicles (FWMAVs) (Supplementary Video 8). Conventional FWMAVs are powered by a tethered a.c. electrical signal with dedicated control, and the wing motion is generated by transmission systems[2,3,30,44,45]. The FLaPTOR wing differs from FWMAVs fundamentally in that (1) remote constant energy induces spontaneous oscillation and (2) the use of self-oscillatory materials as actuators eliminates the need for on-board batteries and transmission-related mass, revolutionizing traditional systems. The FLaPTOR wing was tested under a constrained state when affixed to a hard experimental platform (Fig. 6e, top) and a partially unconstrained state when it was tethered to thin strings (Fig. 6e, bottom). The oscillation performance was $f = 10.5$ Hz and $A = 38°$ under the constrained state, and $f = 9.9$ Hz and $A = 16°$ under the partially unconstrained state. The higher power output for the constrained state was due to less energy transfer and damping to the outer system including the thin strings. To evaluate the wing's capabilities, we used a force transducer set-up to measure the generated thrust (Supplementary Fig. 24)[45]. The FLaPTOR wing could generate an average lift force of 147 μN, with a thrust-to-weight ratio of 0.32, considering the weight of the wing to be 47 mg (Fig. 6f,g). Furthermore, the light power delivered to the oscillating wing was found to be 1.1 W, resulting in a thrust-to-power ratio of 0.13 N kW^{-1}. To compare with other FWMAVs as a reference, the thrust-to-weight ratio and thrust-to-power ratio achieved for the Harvard RoboBee were 1.7 and 41.2 N kW^{-1} (ref. 3). Although the thrust-to-weight ratio needs to exceed 1 for take-off,

https://doi.org/10.1038/s41563-024-02035-3

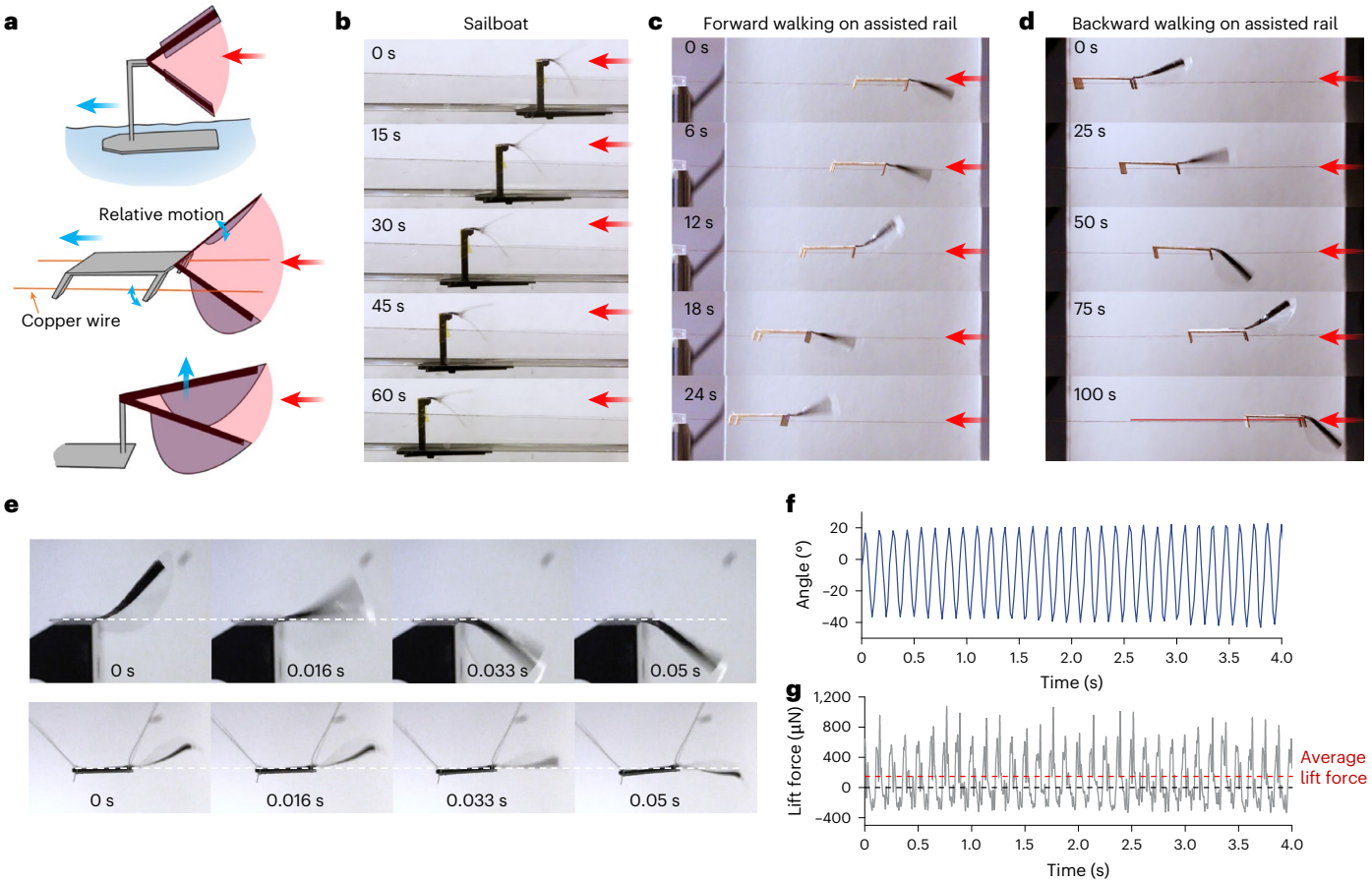

Fig. 6 | Flapping wing application. a,**b**, A schematic representation (**a**) and time-resolved snapshots (**b**) of a sailboat moving on water. **c**,**d**, The forward movement (**c**) and backward movement (**d**) of a FLaPTOR wing-based walker along copper wires. **e**, Time-resolved snapshots of the FlaPTOR wing actuator in one cycle in constraint mode (upper images) and partially unconstrained mode (lower images). The white dashed line marks the horizontal position. **f**,**g**, The angle change (**f**) and generated instant lift force (**g**) of the FlaPTOR wing actuator. The red dashed line indicates the average lift force and the blue dashed line indicates where lift force is zero.

the current results still shows crucial progress towards photo-driven oscillation-based FWMAVs.

In summary, we have developed a high-power-output self-excited oscillator driven by constant light. The oscillator structure consists of an inactive elastomer layer sandwiched by two photo-active LCE layers, reaching a power density comparable to that of insect flight muscles. Such uniquely designed high-performance actuators have shown great promise in powerful autonomous robotics, which require the integration of architecture design, materials innovation, manufacturing and control. Future research, from the standpoint of actuation performance, could focus on further enhancing the photo-thermal energy transduction, the molecular engineering of LCEs to enhance thermomechanical properties and work capacity, the structural design of the FLaPTORs to further increase the power density and improving the actuation efficiency to reduce the light input while maintaining the oscillatory power density. Regarding practical implementations, further studies could incorporate on-board light or other power sources, or a real-time self-correction mechanism to ensure precise and continuous illumination on the FLaPTOR, enhancing the locomotion manoeuvrability and multimodal actuation, and expanding the activation stimuli of FLaPTOR beyond light. These developments promise to broaden the scope of FLaPTOR applications. More importantly, leveraging light-driven autonomous oscillation to enable future hovering applications is both impactful and extremely complex. Achieving this will require sophisticated developments, including highly robust smart materials, light-driven oscillators with higher power density, aerodynamic engineering for efficient lift and system design for synchronized multi-wing hovering.

Online content

Any methods, additional references, Nature Portfolio reporting summaries, source data, extended data, supplementary information, acknowledgements, peer review information; details of author contributions and competing interests; and statements of data and code availability are available at https://doi.org/10.1038/s41563-024-02035-3.

References

1. Rothemund, P. et al. Shaping the future of robotics through materials innovation. *Nat. Mater.* **20**, 1582–1587 (2021).
2. Wood, R. J. The first takeoff of a biologically inspired at-scale robotic insect. *IEEE Trans. Robot.* **24**, 341–347 (2008).
3. Ma, K. Y., Chirarattananon, P., Fuller, S. B. & Wood, R. J. Controlled flight of a biologically inspired, insect-scale robot. *Science* **340**, 603–607 (2013).
4. Hu, L., Zhang, Q., Li, X. & Serpe, M. J. Stimuli-responsive polymers for sensing and actuation. *Mater. Horiz.* **6**, 1774–1793 (2019).
5. Zhao, Y. et al. Stimuli-responsive polymers for soft robotics. *Annu. Rev. Control Robot. Auton. Syst.* **5**, 1–31 (2022).
6. Jeon, S. J., Hauser, A. W. & Hayward, R. C. Shape-morphing materials from stimuli-responsive hydrogel hybrids. *Acc. Chem. Res.* **50**, 161–169 (2017).

7. Zeng, H., Wasylczyk, P., Wiersma, D. S. & Priimagi, A. Light robots: bridging the gap between microrobotics and photomechanics in soft materials. *Adv. Mater.* **30**, 1703554 (2018).
8. Kruse, K. & Jülicher, F. Oscillations in cell biology. *Curr. Opin. Cell Biol.* **17**, 20–26 (2005).
9. Syme, D. A. & Shadwick, R. E. Red muscle function in stiff-bodied swimmers: there and almost back again. *Philos. Trans. R. Soc. B* **366**, 1507–1515 (2011).
10. Gelebart, A. H. et al. Making waves in a photoactive polymer film. *Nature* **546**, 632–636 (2017).
11. Zhao, Y. et al. Sunlight-powered self-excited oscillators for sustainable autonomous soft robotics. *Sci. Robot.* **8**, eadf4753 (2023).
12. Zhao, Y. et al. Soft phototactic swimmer based on self-sustained hydrogel oscillator. *Sci. Robot.* **4**, eaax7112 (2019).
13. Shi, P., Zhao, Y., Liu, Z. & He, X. Liquid crystal elastomer composite-based photo-oscillator for microrobots. *J. Compos. Mater.* **57**, 633–643 (2023).
14. Serak, S. et al. Liquid crystalline polymer cantilever oscillators fueled by light. *Soft Matter* **6**, 779–783 (2010).
15. Lan, R. et al. Near-infrared photodriven self-sustained oscillation of liquid-crystalline network film with predesignated polydopamine coating. *Adv. Mater.* **32**, e1906319 (2020).
16. White, T. J. et al. A high frequency photodriven polymer oscillator. *Soft Matter* **4**, 1796–1798 (2008).
17. Vantomme, G. et al. Coupled liquid crystalline oscillators in Huygens' synchrony. *Nat. Mater.* https://doi.org/10.1038/s41563-021-00931-6 (2021).
18. Li, K. & Cai, S. Modeling of light-driven bending vibration of a liquid crystal elastomer beam. *J. Appl. Mech.* **83**, 031009 (2016).
19. Liang, X., Chen, Z., Zhu, L. & Li, K. Light-powered self-excited oscillation of a liquid crystal elastomer pendulum. *Mech. Syst. Signal Process.* **163**, 108140 (2022).
20. Xuan, C., Zhou, Y., Zhao, Y., He, X. & Jin, L. Photodriven self-excited hydrogel oscillators. *Phys. Rev. Appl.* **17**, 014007 (2022).
21. Shi, P., Zhao, Y., Liu, Z. & He, X. Liquid crystal elastomer composite-based photo-oscillator for microrobots. *J. Compos. Mater.* **57**, 633–643 (2022).
22. Sun, M. & Wu, J. H. Aerodynamic force generation and power requirements in forward flight in a fruit fly with modeled wing motion. *J. Exp. Biol.* **206**, 3065–3083 (2003).
23. Duduta, M., Wood, R. J. & Clarke, D. R. Multilayer dielectric elastomers for fast, programmable actuation without prestretch. *Adv. Mater.* **28**, 8058–8063 (2016).
24. Chen, Y. et al. Controlled flight of a microrobot powered by soft artificial muscles. *Nature* **575**, 324–329 (2019).
25. Zeng, H. et al. Light-fuelled freestyle self-oscillators. *Nat. Commun.* https://doi.org/10.1038/s41467-019-13077-6 (2019).
26. Lee, K. M. et al. Photodriven, flexural-torsional oscillation of glassy azobenzene liquid crystal polymer networks. *Adv. Funct. Mater.* **21**, 2913–2918 (2011).
27. Pringle, J. *Insect Flight* (Cambridge Univ. Press, 1957).
28. Dudley, R. *The Biomechanics of Insect Flight: Form, Function and Evolution* (Princeton Univ. Press, 1999).
29. Helps, T., Romero, C., Taghavi, M., Conn, A. T. & Rossiter, J. Liquid-amplified zipping actuators for micro-air vehicles with transmission-free flapping. *Sci. Robot.* **7**, eabi8189 (2022).
30. Floreano, D. & Wood, R. J. Science, technology and the future of small autonomous drones. *Nature* **521**, 460–466 (2015).
31. Gelebart, A. H., Vantomme, G., Meijer, E. W. & Broer, D. J. Mastering the photothermal effect in liquid crystal networks: a general approach for self-sustained mechanical oscillators. *Adv. Mater.* **29**, 1–6 (2017).
32. Dong, X. et al. Sunlight-driven continuous flapping-wing motion. *ACS Appl. Mater. Interfaces* **12**, 6460–6470 (2020).
33. Qian, X. et al. Artificial phototropism for omnidirectional tracking and harvesting of light. *Nat. Nanotechnol.* **14**, 1048–1055 (2019).
34. Yang, M. et al. Bioinspired phototropic MXene-reinforced soft tubular actuators for omnidirectional light-tracking and adaptive photovoltaics. *Adv. Funct. Mater.* **32**, 1 (2022).
35. Yang, L. et al. An autonomous soft actuator with light-driven self-sustained wavelike oscillation for phototactic self-locomotion and power generation. *Adv. Funct. Mater.* **30**, 1–13 (2020).
36. Vantomme, G., Gelebart, A. H., Broer, D. J. & Meijer, E. W. Self-sustained actuation from heat dissipation in liquid crystal polymer networks. *J. Polym. Sci. A* **56**, 1331–1336 (2018).
37. Zhang, Y. F., Ren, Y. J., Guo, H. C. & Bai, S. L. Enhanced thermal properties of PDMS composites containing vertically aligned graphene tubes. *Appl. Therm. Eng.* **150**, 840–848 (2019).
38. Ford, M. J. et al. A multifunctional shape-morphing elastomer with liquid metal inclusions. *Proc. Natl Acad. Sci. USA* **116**, 21438–21444 (2019).
39. Yang, Y., Pei, Z., Li, Z., Wei, Y. & Ji, Y. Making and remaking dynamic 3D structures by shining light on flat liquid crystalline vitrimer films without a mold. *J. Am. Chem. Soc.* **138**, 2118–2121 (2016).
40. Saed, M. O. et al. Molecularly-engineered, 4D-printed liquid crystal elastomer actuators. *Adv. Funct. Mater.* **29**, 1 (2019).
41. Saed, M. O. et al. High strain actuation liquid crystal elastomers via modulation of mesophase structure. *Soft Matter* **13**, 7537–7547 (2017).
42. Wei, W., Zhang, Z., Wei, J., Li, X. & Guo, J. Phototriggered selective actuation and self-oscillating in dual-phase liquid crystal photonic actuators. *Adv. Opt. Mater.* **6**, 1800131 (2018).
43. Wei, W., Gao, J., Yang, J., Wei, J. & Guo, J. A NIR light-triggered pyroelectric-dominated generator based on a liquid crystal elastomer composite actuator for photoelectric conversion and self-powered sensing. *RSC Adv.* **8**, 40856–40865 (2018).
44. Cao, C., Burgess, S. & Conn, A. T. Toward a dielectric elastomer resonator driven flapping wing micro air vehicle. *Front. Robot. AI* **5**, 1–11 (2019).
45. Mingjing, Q. et al. Asynchronous and self-adaptive flight assembly via electrostatic actuation of flapping wings. *Adv. Intell. Syst.* **3**, 2100048 (2021).

Methods

Materials

LC reactive mesogens RM257 and RM82 were purchase from Shijiazhuang Sdyano Fine Chemical, Co., Ltd. 2,2-(Ethylenedioxy)diethanethiol (EDDET), glycol di(3-mercaptopropionate) (GDMP), 1,6-hexanedithiol (HDT), pentaerythritol tetrakis(3-mercaptopropionate) (PETMP), 1,3,5-triallyl-1,3,5-triazine-2,4,6(1*H*,3*H*,5*H*)-trione (TATATO), I-369, butylated hydroxytoluene (BHT), tetraethyl orthosilicate (TEOS), ammonia solution (30%) and poly(vinylidene fluoride-co-trifluoroethylene) (PVDF-TrFE) (Solvene 250/P400) were purchased from Sigma. Triethylamine (TEA) was used as supplied by EMD. Sylgard 184 PDMS kits were purchased from Ellsworth. Silicone glue (Henkel 908570) was purchased from Amazon.

Materials fabrication

Candle soot (CS) was deposited and collected on aluminium foil above a candle flame. PDMS was made by mixing 5:1 weight ratio of polymeric base and curing agent. PDMS films were fabricated by spin-coating or casting between two glass slides with predefined spacers. We synthesized LCEs by three methodologies. For DIW-TE LCEs, a thiol–ene click reaction was used with modified chemistry[40]. The oligomerization of ink was completed for 3 h at 65°C, and the as-printed samples were post-crosslinked under ultraviolet (UV) light for 5 min on two sides. For MeS-TE LCEs, mechanical stretching was used to increase the mesogen alignment, and the samples were stretched to monodomain and irradiated under UV light to trigger thiol–ene crosslinking for 30 min along two sides. For MeS-TA LCEs, the Yakacki[46] method was used to synthesize the samples, and the first stage of thermal oligomerization was completed overnight at room temperature. The samples were then uniaxially stretched to a monodomain state and irradiated under UV light to complete the diacrylate crosslinking for 2 h in total.

FLaPTOR fabrication

A thin layer of silica coating was grown on LCE by room-temperature chemical vapour deposition to ensure good adhesion between the LCE and PDMS. To create the trilayer structure, PDMS film was sandwiched by two silica-coated LCEs with silicone glue in between. The proprioceptive oscillator was fabricated by laser cutting PDMS into a pattern, sputtering gold for 120 s on the PDMS and sandwiching it between two LCE films with silicone glue/hexane solution. The piezoelectric/pyroelectric nanogenerator was built using PVDF-TrFE as an active layer and two gold layers as electrodes with a capacitive configuration, and sandwiched by PDMS and LCE using silicone glue. For the FLaPTOR wing structure, PET was laser cut into predesigned wing structures. Then, the multilayer wing was laminated by LCE, PDMS, PET, PDMS and LCE, sequentially. The interface between each layer was glued with silicone glue to enhance the adhesion.

Characterization

The thermomechanical properties of the LCEs were measured by using a dynamic mechanical analyser. The LCEs underwent annealing and cooling to remove thermal history before testing. The modulus, actuation strain and stress, and work capacity were measured by using a DMA850. To characterize the oscillations, trilayer structures were mounted on a stage and exposed to light. The light triggered out-of-equilibrium oscillation, and the trilayer reached a steady state. The oscillation behaviour was recorded with a camera, and the tip angle was measured by Tracker software to calculate the frequency, amplitude and power density.

Data availability

All data needed to evaluate and support the conclusions in the paper are included in the main text or Supplementary Information.

Reference

46. Saed, M. O. et al. Thiol-acrylate main-chain liquid-crystalline elastomers with tunable thermomechanical properties and actuation strain. *J. Polym. Sci. B* **55**, 157–168 (2017).

Acknowledgements

The research was supported by AFOSR awards FA955017-1-0311 and FA9550-20-1-0344 and ONR awards N000141712117, N000141812314 and N000142412187. We thank W. Yan for his participation in discussions and assistance with equipment set-up.

Author contributions

X.H. conceived the concept and supervised the research. X.H. and Y.Z. designed this project. Y.Z., P.S. and C.C conducted the fabrication and characterization of materials, including LCE, PDMS, CS, adhesives, electrode sputtering, PVDF and so on. Y.Z., Y.A. and Y.Y. set up all the experimental equipment and systems for fabrication and characterization, including the optical equipment, DIW printing, spin coating, sonication, DMA, IR camera and so on. Y.Z., P.S., C.C., Y.A. and Y.Y. conducted characterizations of oscillators and data analysis, accordingly. Z.L. developed all the simulations and theory under supervision. All authors wrote the paper. All authors have given approval to the final version of the paper.

Competing interests

The authors declare no competing interests.

Additional information

Supplementary information The online version contains supplementary material available at https://doi.org/10.1038/s41563-024-02035-3.

Correspondence and requests for materials should be addressed to Ximin He.

Peer review information *Nature Materials* thanks Xueju Wang and the other, anonymous, reviewer(s) for their contribution to the peer review of this work.